



TECHNICAL ARTICLE

Effect of Cracks on Thermal Shock Behavior of Plasma-Sprayed Thick Thermal Barrier Coatings

Shiqian Tao, Jiasheng Yang, Fang Shao, Huayu Zhao, Xinghua Zhong, Yin Zhuang, Jing Sheng, Jinxing Ni, Qinghui Li, and Shunyan Tao

Submitted: 20 February 2022 / Revised: 30 August 2022 / Accepted: 30 August 2022 / Published online: 12 October 2022

Only a few of the numerous studies on plasma-sprayed thick thermal barrier coatings (TTBCs) have focused on the relationship between the thermal shock resistance of the TTBCs and cracks in the ceramic coating. In this study, three types of TTBCs (a traditional coating, nanostructured coating, and segmentation-cracked coating) with different intrinsic cracks were deposited via atmospheric plasma spraying (APS). To analyze the failure mechanism of these thick coatings, the correlations among the phase composition, microstructure, grain growth behaviors, mechanical properties, and stress distribution were investigated using scanning electron microscope, X-ray diffraction, electron back-scattered diffraction, Raman spectroscopy and Vickers hardness tester. The results showed that numerous newly generated vertical cracks in the underlying part of the ceramic topcoat of a TTBC contributed to the release of the accumulated residual stress, thereby improving the thermal shock resistance. The failure mechanism of TTBCs deposited using APS was most likely dominated by residual stresses generated as a result of the thermal expansion mismatch originating from adjacent parts such as the substrate and bond coat, and the bond coat and topcoat. This led to the initiation and propagation of cracks, and finally the peeling of the thick coating.

Keywords microcrack, plasma spraying, residual stress, thermal shock resistance, thick thermal barrier coatings

1. Introduction

In the past five decades, plasma-sprayed thermal barrier coatings (TBCs) have been increasingly applied to the hot sections of aircraft engines and gas turbines to protect metallic components from thermal loads by decreasing the surface temperature of the substrate, thereby greatly enhancing the working efficiency and performance (Ref 1-4). Traditionally, a standard double-layered TBC system consists of a thermal insulation ceramic topcoat over a transitional and oxidation-resistant bond coat. To provide a high thermal expansion coefficient that matches the substrate, along with low thermal conductivity and good thermal shock resistance, 6-8 wt.% yttria-stabilized zirconia (YSZ) is increasingly being applied in

ceramic coatings (Ref 5, 6). Apart from acting as a cooling gas film, a typical thin TBC can only reduce the substrate surface temperature by approximately 170 °C during service (Ref 7).

The thermal insulation performance of a TBC is proportional to the thickness of the ceramic layer (Ref 8). Increasing the coating thickness is one of the most effective and successful ways to develop a TBC with an excellent thermal insulation performance and a longer service life (Ref 9, 10). However, thick thermal barrier coatings (TTBCs) prepared by the traditional atmospheric plasma spraying (APS) process have lower thermal shock resistances and bond strengths. As reported, long-term spraying causes a larger temperature gradient in each layer and greater residual stress inside the ceramic coating, which increases the thermal mismatch stress originating from the difference in the thermal expansion coefficients of neighboring layers of the TTBC system (Ref 11-13). Various measures have been taken to address these difficulties, including altering the spraying parameters or employing a variety of powders with distinctive size distributions and morphologies to produce dense coatings, segmented coatings, columnar-like coatings, gradient structured coatings, and mixed microstructure coatings (Ref 14-17). Coatings with distinguishing structures have manifested different characteristics. Segmentation-crack-structured TTBCs combine the advantages of higher strain tolerance and better thermal insulation properties. This can be attributed to the fact that the intrinsic cracks not only inhibit the extension and propagation of horizontal cracks, but also efficaciously relieve the accumulated residual stress generated during thermal shock tests, ultimately improving the strain tolerance (Ref 18, 19). Several studies have focused on the stress state and crack evolution in plasma-sprayed TBCs subjected to thermal fatigue or isothermal heat treatment (Ref 20-25). However, studies have rarely focused on the effect of microstructural features on the thermal shock

Shiqian Tao, Laboratory of Micro-Nano Optoelectronic Materials and Devices, Shanghai Institute of Optics and Fine Mechanics, Chinese Academy of Sciences, Shanghai 201800, China; Key Laboratory of Inorganic Coating Materials CAS, Shanghai Institute of Ceramics, Chinese Academy of Sciences, Shanghai 201899, China; and University of Chinese Academy of Sciences, Beijing 100049, China; **Jiasheng Yang**, **Fang Shao**, **Huayu Zhao**, **Xinghua Zhong**, **Yin Zhuang**, **Jing Sheng**, **Jinxing Ni**, and **Shunyan Tao**, Key Laboratory of Inorganic Coating Materials CAS, Shanghai Institute of Ceramics, Chinese Academy of Sciences, Shanghai 201899, China; **Qinghui Li**, Laboratory of Micro-Nano Optoelectronic Materials and Devices, Shanghai Institute of Optics and Fine Mechanics, Chinese Academy of Sciences, Shanghai 201800, China. Contact e-mails: jiashengyang@mail.sic.ac.cn and sytao@mail.sic.ac.cn.

resistance of TTBCs, much less on a systematic comparative study of the crack evolution (e.g., crack size, distribution, density, and location) of lamellar and segmented structured thick coatings. Thermal shock resistance is an important index for evaluating the quality of barrier coatings in high-temperature thermal shock environments. A sudden temperature difference causes a large thermal stress in the ceramic layer, which induces the initiation and propagation of cracks and finally the failure of the coating. Therefore, it is important to conduct thermal shock tests for thick thermal barrier coatings in practical engineering applications.

In this work, three types of YSZ TTBCs were prepared using the APS process and adopting conventional micron-sized powder and nano-agglomerated powder, with the goal of investigating the relationship between the thermal shock behavior of the TTBCs and cracks in their ceramic topcoats. The microstructure evolution, phase composition, grain growth, mechanical properties, and stress distribution of each as-sprayed coating and sample subjected to thermal shock were investigated using a variety of characterization methods. A comparative analysis of the failure mechanisms of the TTBCs deposited using APS was conducted. This scientific research may provide theoretical guidance for the engineering applications of thick coatings.

2. Materials and Methods

2.1 Coating Preparation

The TBC system comprised three primary parts: (a) a GH3128 superalloy 25 mm × 25 mm × 2.7 mm substrate (Ni-20Cr-8Mo-8 W-0.5Al-0.5Ti); (b) an approximately 150- μ m-thick CoNiCrAlY bond coat (Amdry 9951, Oerlikon Metco), prepared by vacuum plasma spraying (VPS, Oerlikon Metco, Wohlen, Switzerland); and (c) an adiabatic (ZrO₂-8 wt.% Y₂O₃) ceramic-coat, prepared using an atmospheric plasma spraying system (Oerlikon Metco, Wohlen, Switzerland) equipped with a common F4MB-XL plasma gun. The thicknesses of the as-prepared ceramic coatings (samples N1, N2, and N3 were made of commercially available ceramic powders P1, P2, and P3, respectively) were approximately 1.25 ± 0.10 mm, 1.15 ± 0.05 mm, and 1.10 ± 0.10 mm, respectively. Powders P1 and P2 were conventional micron-sized powders with different size distributions, and powder P3 was a nano-agglomerated powder. The narrow range and small size aggregates were fully heated in the plasma jet to produce a molten coating with lower porosity. High-density and spherical agglomerates were also heated in the plasma jet, contributing to a more compact nano-micron double-state structure inside the coating (Ref 26, 27). Table 1 lists the chemical composition and size distribution of each metal and ceramic powder used for the

bond coat and YSZ topcoat. Table 2 lists the specific spraying parameters. Scanning electron microscopy (SEM) images and x-ray diffraction (XRD) results are shown in Fig. 1. The substrate was then preheated to 300 °C.

2.2 Thermal Shock Test

The three groups of samples were tested in a tube furnace (SLG 1400-50, Shanghai Shengli Test Instrument Co., Ltd., China) by following three different heating regimes (RT-900 °C: 9 °C/min; 900-1100 °C: 5 °C/min; maintained at 1100 °C for 30 min) and water quenching (the coating samples were directly dropped into deionized water at approximately 25 °C). Images were taken, and the corresponding morphological changes were recorded after every five experiments. The same procedure was repeated until 10% of the coating surface peeled off, and the number of cycles before spallation and exfoliation was considered to be the thermal shock lifetime of that coating sample. This thermal shock test helped us to understand the appearance and microstructure variation of the TTBC systems with substrates deposited using APS under abrupt temperature changes.

2.3 Microstructure Characterization

The surface and cross-sectional morphologies of the thick coatings were examined using a scanning electron microscope (S-4800, HITACHI, Tokyo, Japan) to obtain backscattered and secondary electron image patterns. The phase compositions of the three types of TTBCs deposited using APS before and after the thermal shock tests were determined using an x-ray diffractometer (D/max 2550 V, Rigaku Industrial Corporation, Japan) with filtered Cu K α radiation (40 kV, 40 mA). This specific information was acquired during a routine inspection (scanning speed: 4° min⁻¹; scanning area: 10-90°). More detailed characteristics, such as the phase component, morphology, distribution, orientation, and crystalline grain growth behavior were systematically investigated using electron

Table 2 Spray parameters for bond coat and ceramic topcoat deposited using plasma spraying process

Spray parameters	Bond coat	Topcoat
Plasma torch	O3CP	F4-MB
Plasma gas mixture	Ar + H ₂	Ar + H ₂
Plasma gas flow rate, slpm	Ar: 100-110 H ₂ : 4-7	Ar: 35-40 H ₂ : 7-9
Carrier gas, slpm	5	3.5-4.0
Stand-off distance, mm	330-370	70-80
Powder feed rate, g/min	35-45	35-40
Power, kW	100-110	40-43
Current, A	1700-2000	620-630

Table 1 Chemical composition and size distribution of each metal and ceramic powder

Powder	Chemical composition, wt.%	Granulometric distribution
Amdry 9951	Co-32Ni-21Cr-8Al-0.5Y	5.5-38 μ m
P1	ZrO ₂ -8Y ₂ O ₃	15-45 μ m
P2	ZrO ₂ -8Y ₂ O ₃	20-90 μ m
P3	ZrO ₂ -8Y ₂ O ₃	45-75 μ m

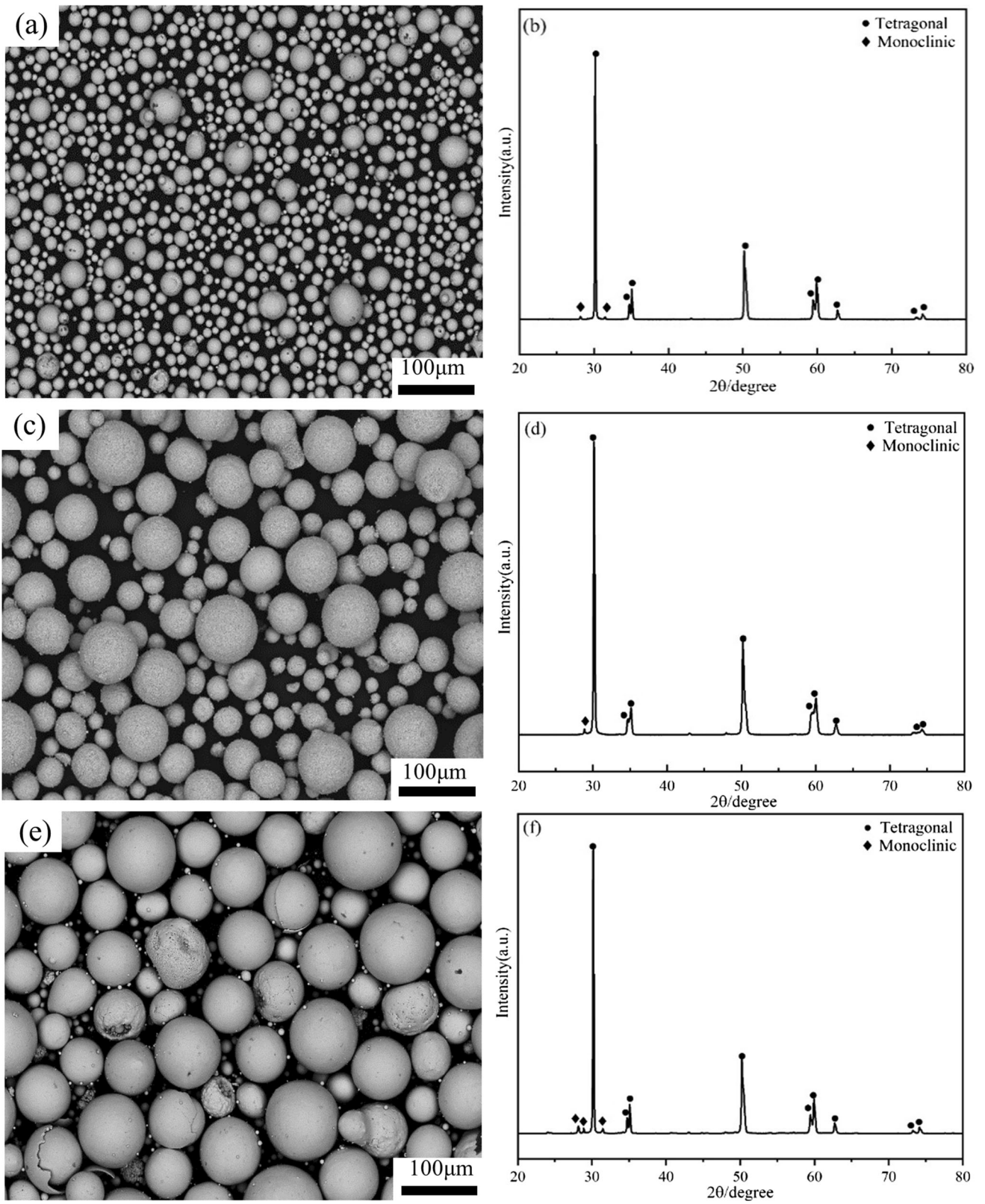


Fig. 1 Morphologies and phase compositions of three types of 8YSZ ceramic powders for the topcoat: (a, b) P1 powder, (c, d) P2 powder, and (e, f) P3 powder

backscatter diffraction (EBSD, NordlysNano, Oxford, UK). All the specimens along with the substrates were cut into small pieces to meet different test requirements. For cross-sectional observations, some samples required impregnation within epoxy resin (conductive resin for EBSD), followed by further grinding and elaborate polishing. In addition, the samples prepared for EBSD testing required further processing using an ion-milling device (EM TIC3X, Leica, Germany). Energy dispersive x-ray spectrometry (EDS, SwiftED3000, Oxford Instruments, UK) was used to analyze the elemental composition of the thermally grown oxide (TGO) layer.

2.4 Mechanical Property

The Vickers microhardness values of the as-sprayed coatings and samples subjected to thermal shock were measured using a hardness tester (Vickers, Tukon-2100B, Instron, USA) under a load of 300 g with a dwelling time of 10 s. All the coating samples were mounted in vacuum with epoxy resin, cut to meet the measurement needs, and then ground and finely polished using routine metallographic methods. The cross sections had to be kept flat. During the experiments, approximately 15 readings were taken at different positions for each specimen, and the average Vickers hardness of each sample was calculated.

2.5 Stress Measurement by Micro-Raman Spectroscopy

Residual stress measurements were performed using a confocal Raman microprobe system equipped with 532 nm laser excitation (Renishaw InVia Confocal micro-Raman Microscope, Gloucestershire, UK). In principle, if the ceramic top coat possessed residual stress, the YSZ characteristic peaks would be sensitive to this stress concentration, resulting in a band shift and deformation. In this work, we performed a comparative analysis of the stress distributions of the N2 and N3 coatings, including the residual stress along the coating thickness and in the underlying part of the ceramic layer near the topcoat/bond coat interface (20–30 μm). Raman spectroscopy was performed in the range of 100–800 cm^{-1} . The Raman peak at approximately 638 cm^{-1} had a prominent intensity, which was used to calculate the stress distribution in the 8YSZ ceramic topcoat because it had a good signal-to-noise ratio. In a TTBC system deposited using APS, σ (MPa) is usually defined as the residual stress and can be calculated using the following equation (Ref 28):

$$\sigma_{\text{TBC}} = (V_o - V_{\text{TBC}}) \cdot \pi_{\text{TBC}},$$

where π_{TBC} is the piezo-spectroscopic coefficient (40 $\text{MPa} \cdot \text{cm}^{-1}$); V_o is the Raman shift peak for the 8YSZ powder (637.35 cm^{-1}); and V_{TBC} is the Raman shift peak at the measurement position for the coating.

3. Results and Discussion

3.1 Microstructure of As-Sprayed TTBCs

Figure 2 presents the polished cross-sectional morphologies of the as-sprayed N1, N2, and N3 coatings. Based on image analysis, the N1 TTBC was characterized by a unique structure of vertical cracks perpendicular to the coating surface and branching cracks parallel to the coating surface. In general,

vertical cracks that penetrate at least half of the coating thickness are referred to as segmentation cracks, and an important parameter defined as the segmentation crack density (D_s) has a decisive impact on the thermal shock lifetime of the coating. The estimated D_s of the N1 TTBC was approximately 2.5 mm^{-1} , and the crack gap was approximately 3 μm . In contrast to the N1 coating, some visible vertical and horizontal cracks existed in the upper part of the N2 TTBC (near the surface of the ceramic topcoat), and their structures were much more compact. There was no continuous segmented area in the top coat close to its interface with the bond coat. In addition, no bridging or penetration was observed between the cracks. For comparison, the N3 coating exhibited a distinctive characteristic with a typical stratified structure (splat boundaries and lamellar interfaces), which can frequently be seen in traditional thin TBCs deposited using APS. The loose stacking between the splats facilitated the formation of interlayer pores and microcracks. As mentioned, the crack state not only showed a strong dependence on the spraying conditions (substrate temperature, stand-off distance, and spray power), but also on the difference in feedstocks (morphology, grain size, and fluidity). The influence of the powder morphology and size distribution on the coating structure was mainly reflected in the temperature and velocity of the droplets before they collided with the substrate (Ref 29–32). The effect of particle size was embodied in three ways: (1) it affected the ability of the powder to enter the plasma flame; (2) it affected the heating and acceleration characteristics of the powder in the plasma flame; and (3) it influenced the competitive relationship between the cooling and solidification processes and the spreading process after droplets impacted on the substrate. A large number of particles entered the plasma flame during spraying; therefore, the size distribution of the powder was extremely important. The powder morphology directly influenced the effects of the carrier gas and plasma flame on the particles. It should also be noted that a certain density of vertical cracks can not only inhibit the consecutive propagation of branching cracks but can also effectively alleviate the thermal stress produced in extremely harsh environments, thereby prolonging the service lifespan and improving the reliability of the coatings.

The EBSD results provided much more detailed information than the SEM, such as the phase composition, grain size, and features of the defects (microcracks and micropores). The diverse colors in the images represent the differentiable phase content. The red, blue, and black areas indicate the tetragonal phase (t-ZrO₂), monoclinic phase (m-ZrO₂), and defects in the coating, respectively. As can be seen, the as-sprayed coatings mainly consisted of a tetragonal phase, given the rapid cooling and solidification of the in-flight YSZ particles, restricting yttrium diffusion. The existence of m-ZrO₂ was mainly related to the unmelted and semi-melted particles in the coating. It was evident that the microstructure features in the three samples corresponded to plentiful dense columnar grains but were quite distinct in character. As shown in Fig. 3, the N1 TTBC presented inter- and intra-microcracks and finer pores, and crystalline grains were closely connected, with some growing through the lamella thickness. Such vertical cracks in the N2 TTBC were initiated during plasma spraying on account of stress remission, and the crack distribution was non-directional. Many defects were recognizable in the microstructure of N3 TTBC, such as the absence of bonding between the splats and significant porosity. Grain growth showed no preferred orientation in the TTBCs deposited using APS, regardless of the

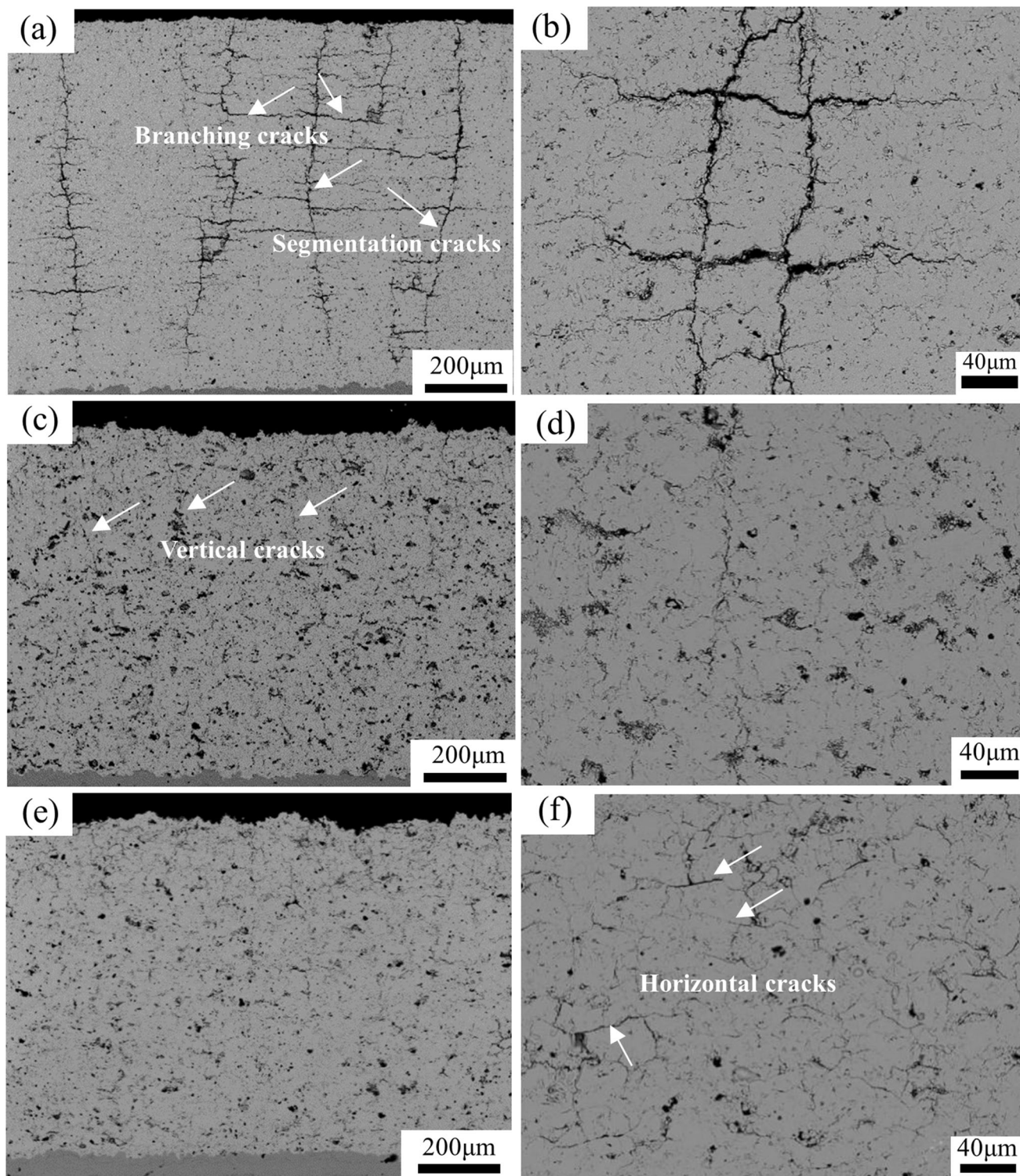


Fig. 2 Polished section morphologies (at low (left) and high (right) magnification) of as-deposited TTBCs: (a, b) N1 coatings, (c, d) N2 coatings, and (e, f) N3 coatings

coating microstructure. Table 3 summarizes the parameters of the three types of as-sprayed TTBCs obtained from the EBSD data, such as the grain size and the contents of t-ZrO₂ and m-ZrO₂.

To describe the grain behavior more specifically, Fig. 4 shows the statistical results for the crystalline grain diameter acquired from the EBSD analysis. The average grain sizes of

the as-deposited N1, N2, and N3 TTBCs were approximately 0.846, 1.055, and 0.791 μm , respectively. The N2 coating had the clearest grain boundaries, whereas the N3 coating had the highest total grain boundary density. Feedstocks with different size distributions accelerated this distinction. The grains in the coating were mainly classified into three types: columnar, equiaxed, and large-scale grains. In the process of plasma

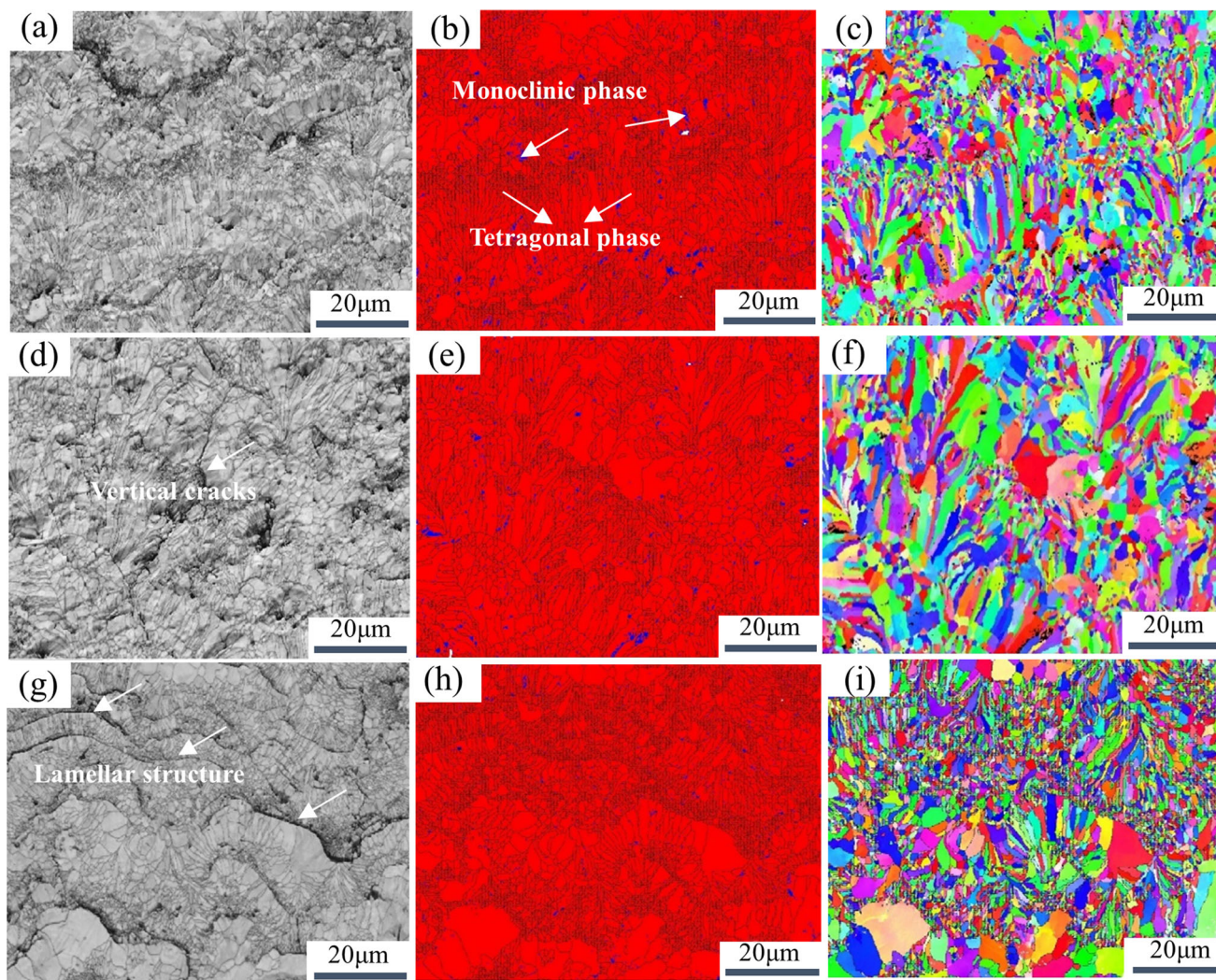


Fig. 3 EBSD test results of as-deposited TTBCs: (a, d, g) band contrast maps, (b, e, h) phase maps, (c, f, i) orientation maps, (a–c) N1 coating, (d–f) N2 coating, and (g–i) N3 coating

Table 3 Phase constitution and corresponding grain size of each as-sprayed thick coating

Coating	Tetragonal phase, T/%	Monoclinic phase, M/%	Grain size, μm
N1	98.4	1.61	T: 0.854 M: 0.563 T + M: 0.846
N2	98.6	1.36	T: 1.070 M: 0.607 T + M: 1.055
N3	99.3	0.68	T: 0.792 M: 0.525 T + M: 0.791

spraying, the molten particles easily formed columnar crystals, and the unmelted or semi-melted particles had a tendency to generate equiaxial crystals. Individual large-sized grains with multilateral boundaries had a strong connection to smaller grains with random orientations, restricting and strengthening each other. The bridging structure between the small-scale grains facilitated the hysteresis effect of the segmented and horizontal cracks. The energy for crack penetration and

propagation increased markedly to modify and improve the thermal shock resistance. In contrast to the N1 and N2 TTBCs, the N3 TTBC possessed a narrow range of grain size distribution.

3.2 Thermal Shock Behavior

Figure 5 shows the thermal shock cycling lifetimes of N1, N2, and N3 coatings. In addition, the corresponding macro-

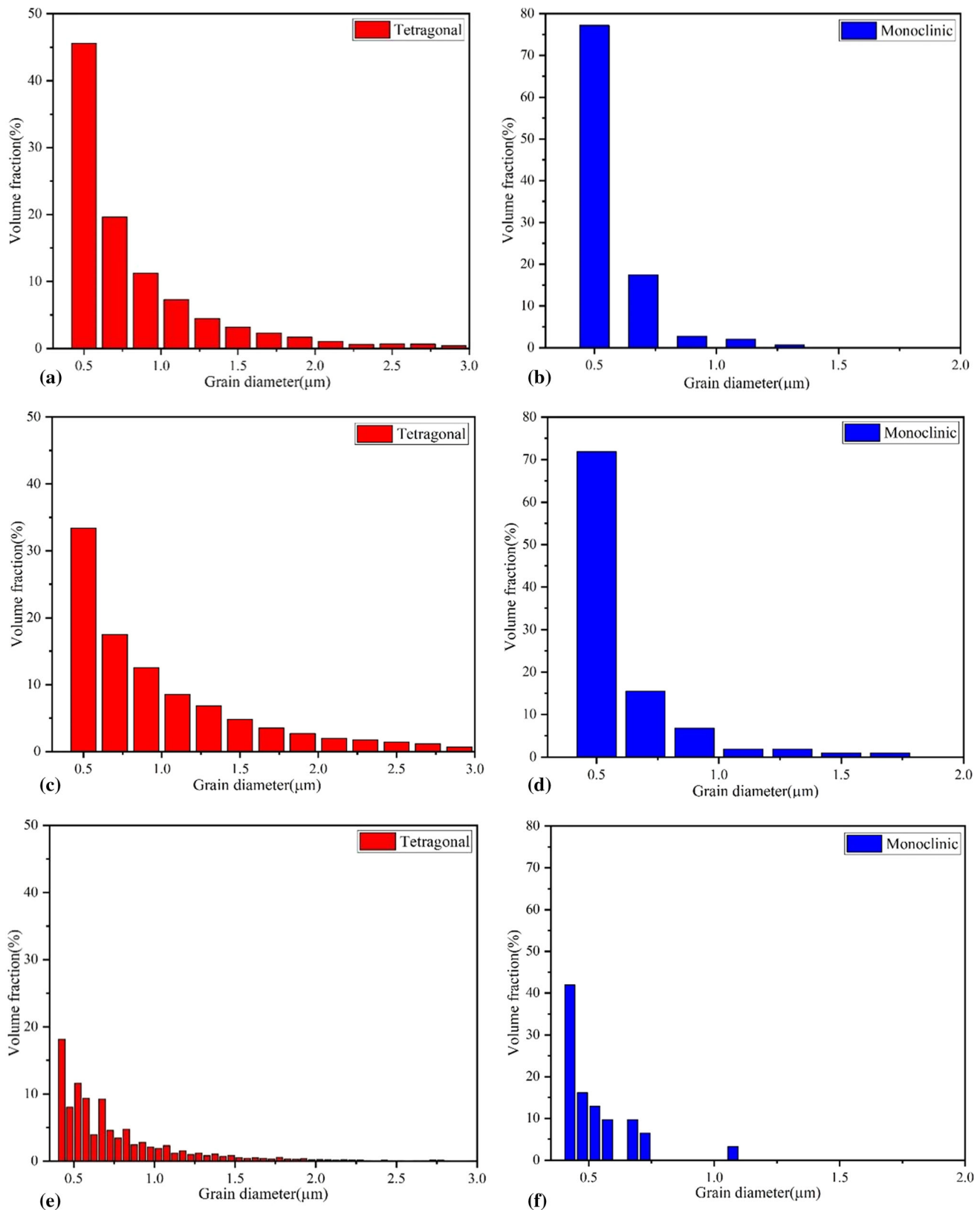


Fig. 4 Crystalline grain size distributions of as-sprayed thick coatings: (a, b) N1 TTBCs, (c, d) N2 TTBCs, and (e, f) N3 TTBCs. (The statistical results for the crystalline grain diameters were acquired from the EBSD analysis. Generally, irregular crystal grains were considered equivalent to an effective circle for processing, and the effective area and effective diameter were used for the calculation.)

scopic features during thermal shock were well documented, as shown in Fig. 6. As can be seen, the edge spallation of N1 TTBC began after 10 cycles and then suffered from a complete shedding after 11 cycles. The N2 coating exhibited the longest thermal shock lifetime. It was subjected to damage after 65 cycles, and the border areas gradually broke up on further cycling, accompanied by propagation to adjacent areas. Finally, exfoliation of more than 10% occurred after 81 cycles. Similar to the failure process of N2 TTBC, the observed cracking of N3 TTBC began at the edge and progressed toward the center. Apparently, the thermal shock lifetimes of N1 and N3 coatings were similar, but the microstructures were significantly different. The extended lifetimes of N2 TTBC could be attributed to the increased Ds and superior nanostructured region in the coating, which were beneficial for the relieving of thermal mismatch stress, restraining crack propagation along the crystalline crystals, strengthening the coating durability, and prolonging the service life.

3.3 Phase Composition

A 6-8 wt.% YSZ, used as a ceramic coating material, experiences a tetragonal–monoclinic phase transformation when the temperature is higher than 1250 °C. This process is usually associated with a volume expansion of up to 3-5% (Ref 33, 34). Such irreversible decomposition could decrease the integrity of the coating and generate thermal stress, eventually leading to the peeling of the TTBC. Based on the XRD spectra displayed in Fig. 7, the primary phase component of the three types of as-sprayed coatings was the non-equilibrium tetragonal phase (t' -ZrO₂), and no m -ZrO₂ phase was generated during the thermal shock tests, demonstrating that phase transformation was not the dominant failure mechanism of the TTBCs deposited using APS, which was consistent with the qualitative analysis results provided thus far. That t' peaks were noticed to slightly deviate to the left for the thermally cycled N2 and N3

coatings. Based on the Bragg equation, the interplanar spacing is the governing factor that changes the diffraction angle. The comparison of the XRD patterns of the as-sprayed and failed samples revealed that the residual stress rather than Y³⁺ diffusion potentially caused severe damage to the TTBC system. In addition, the offset of N2 TTBC was larger than that of N3 TTBC, which may account for the higher residual stress level generated by the thermal mismatch during the tests. The lack of movement in N1 coating may give credence to this failure mode, and integral spallation of the ceramic topcoat relaxed the residual stress. The significant changes in the peak intensity could be explained by lattice distortion resulting from uneven heating during the atmospheric plasma spraying process. The Raman spectra of the as-sprayed and thermally shocked samples (using N2 and N3 coatings as examples) are shown in Fig. 8. The results demonstrated that there was no phase transition in the coatings before and after the thermal shock. In the range of 100-800 cm⁻¹, the characteristic spectral line of the tetragonal phase rather than the monoclinic or cubic phase was observed, which was consistent with the XRD results.

3.4 Microstructure

Figure 9 shows the cross-sectional microstructures of the thermally shocked N1, N2, and N3 coatings. The different morphologies indicate different failure modes. N1 TTBC showed progressive delamination, which was initiated by inherent crack propagation and bridging. The horizontal cracks proceeded toward the coating center and gradually merged with the inner vertical or segmentation cracks, widening under thermal stress, until the coating ultimately failed in the topcoat. N2 TTBC showed no apparent failure in the microstructure, indicating that it had a superior thermal shock characteristic. The numerous newly generated vertical cracks at the underlying layer of the ceramic topcoat helped to improve the strain

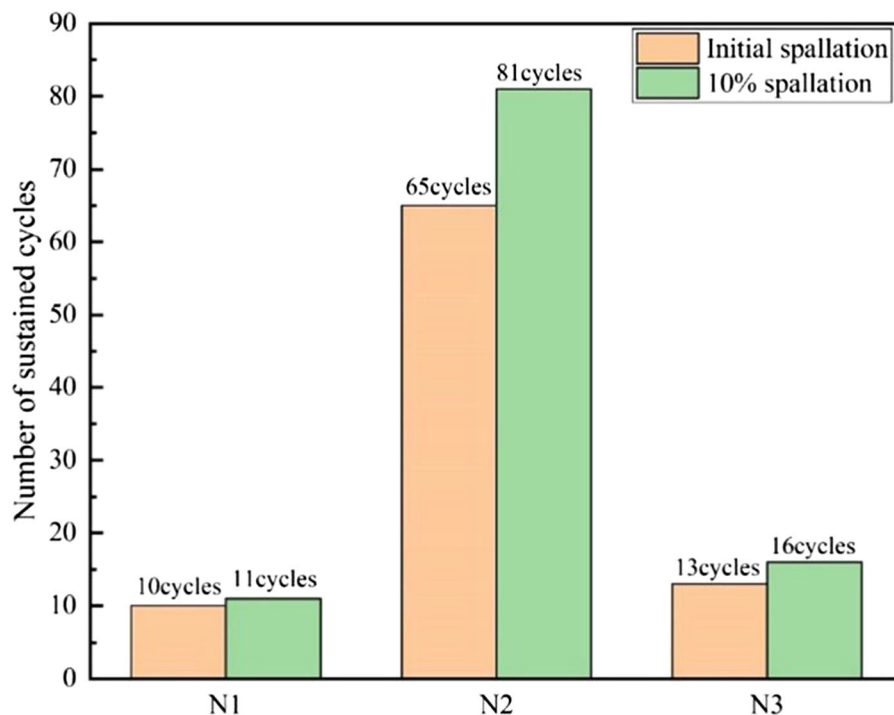
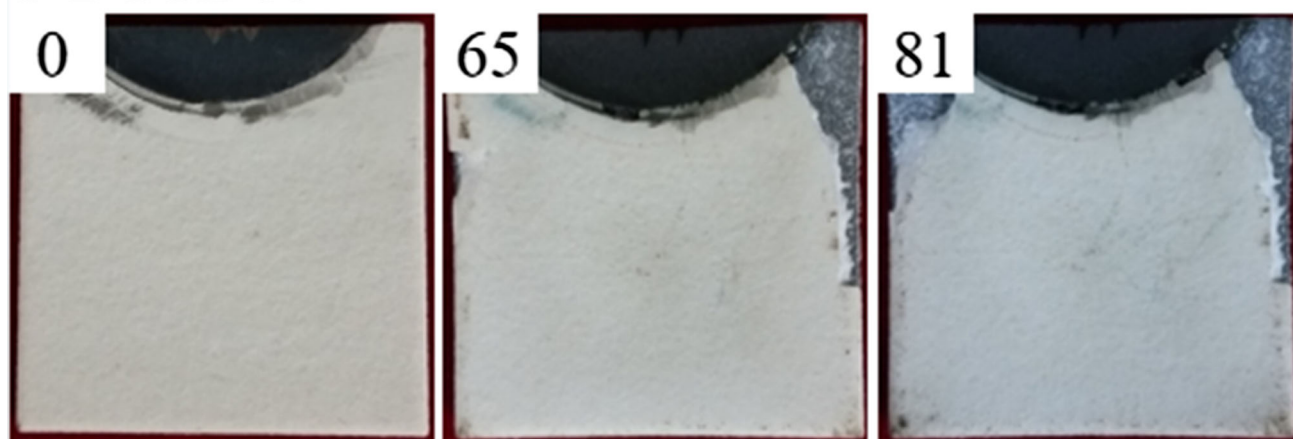


Fig. 5 Number of sustained cycles with three kinds of TTBCs, where the thermal shock temperature was 1100 °C

N1 TTBCs



N2 TTBCs



N3 TTBCs

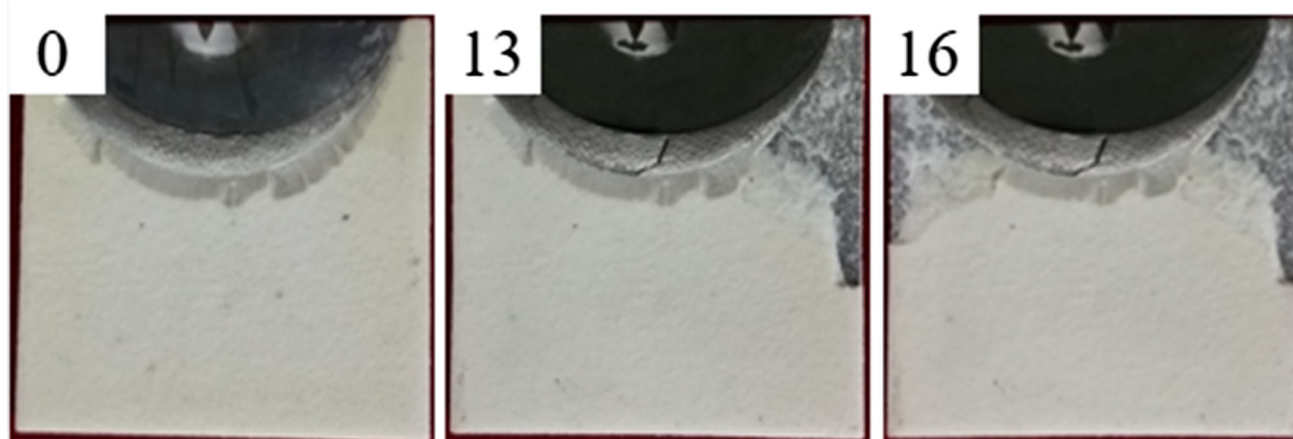


Fig. 6 Macroscopic morphology features of N1, N2, and N3 coatings during thermal shock tests, where the thermal shock temperature was 1100 °C

tolerance of the coating. The short thermal shock lifetimes of N3 TTBC were closely related to the microstructure. The intrinsic lamellar structure reduced the bonding strength of the TBC system because abrupt temperature changes accelerated the thermal expansion mismatch between the top coating and substrate. On the other hand, inadequate vertical cracks did not

help to alleviate the thermal stress, eventually giving rise to the low strain tolerance of the APS coatings, and the occurrence rate of premature failure was much larger under a thermal shock condition (Ref 35-37). Both N2 and N3 TTBCs mainly failed at the ceramic layer near the interface between the topcoat and bond coat. The mismatch of thermal expansion coefficients

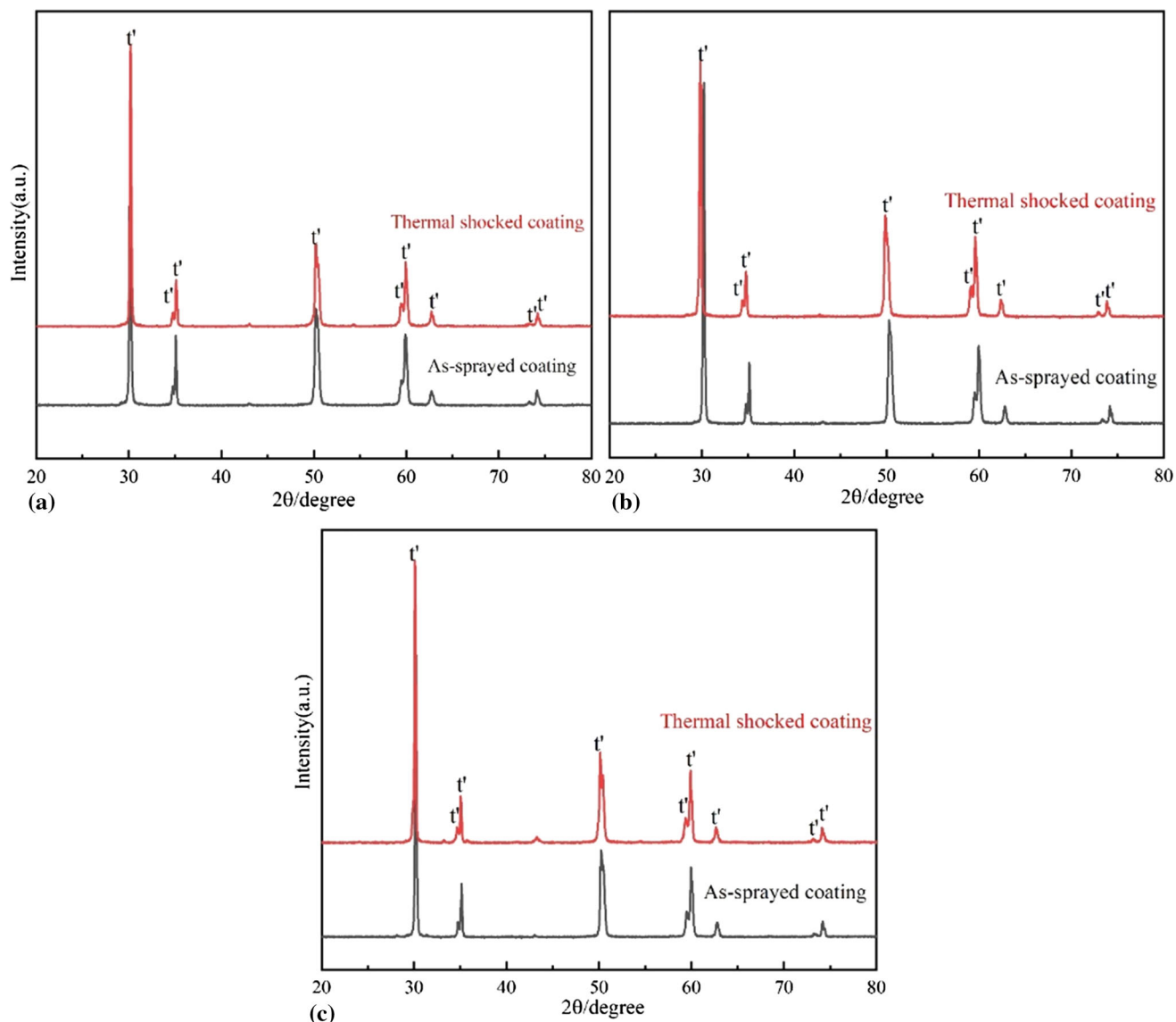


Fig. 7 XRD results for three groups of coating samples before and after thermal shock tests: (a) N1 TTBCs, (b) N2 TTBCs, and (c) N3 TTBCs

between the neighboring parts led to a residual stress accumulation, accelerated microcrack nucleation and propagation, and a continuous negative influence on the lifetime of the coating.

An analysis of the bond coat (BC)/topcoat interface (Fig. 10) revealed that rumpled TGO layers formed in all the samples with different thicknesses. The thicknesses of the TGO layers of the thermally shocked N1, N2, and N3 coatings were approximately 1-3, 5-8, and 0.5-1 μm , respectively. The oxidation of N2 TTBC was the most severe, while that of N3 TTBC was the lowest. The elemental distribution at the interface is shown in Fig. 11, where the dark black TGO is mainly composed of Al_2O_3 . This result supported the hypothesis that the oxidation behavior of the CoNiCrAlY BC influenced the lifetime of the TTBC, and that the outward diffusion of aluminum from the BC toward the interface produced a chemical reaction with the incoming oxygen and contributed to the TGO formation. The thickening and growth of the TGO may have aggravated the thermal expansion mismatch between the ceramic topcoat and metallic substrate

during the heating and cooling thermal shock conditions, accompanied by the continuous intrinsic degradation of the TBC system (Ref 38, 39). Another noteworthy phenomenon showed that some mixed radial and horizontal cracks were generated close to the BC and TGO growth in N2 coatings, whereas a large number of horizontal cracks formed in N3 coating, which promoted the inter-connection of cracks under thermal stress, eventually causing the detachment of the coating as a result of the edge effects. Compared to the other coatings, the severe oxidation of N2 BC was due to the following three factors: (1) the N2 TTBC with improved D_s values increased the passage for oxygen transmission through the ceramic topcoat; thus, the BC underwent severe oxidation when exposed to higher temperatures; (2) N2 TTBCs with higher D_s values exhibited improved thermal shock resistance, which in turn prolonged the oxidation time; and (3) the intergranular fracture in the nanostructured N2 TTBCs limited the extension and penetration of microcracks because there was a longer pathway for crack growth. It is worth mentioning that although

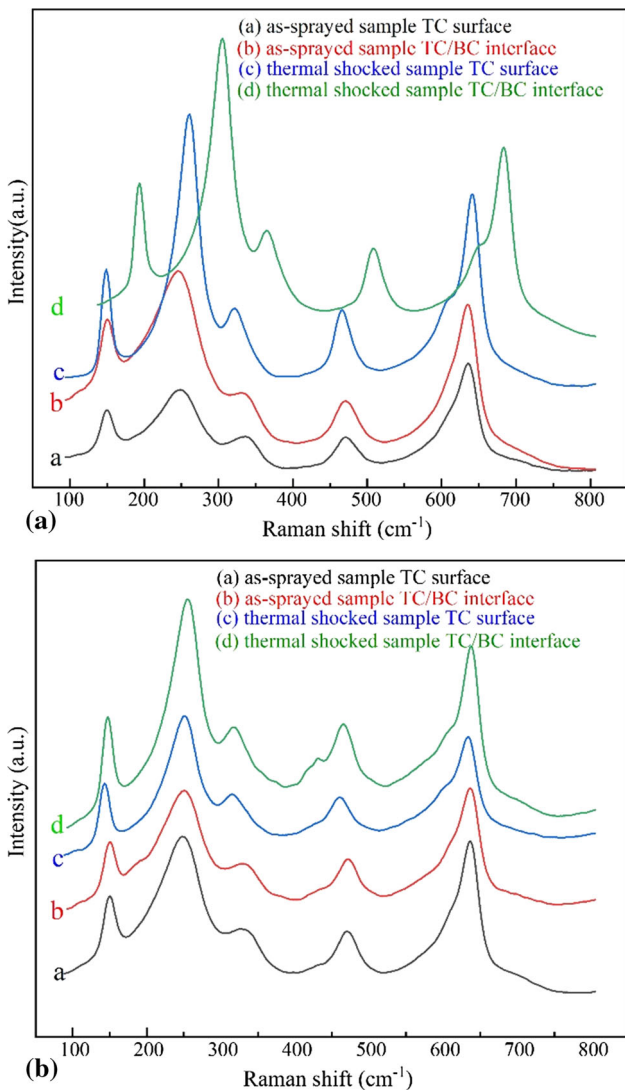


Fig. 8 Raman spectra of two groups of coating samples before and after thermal shock tests: (a) N2 TTBCs and (b) N3 TTBCs

N1 TTBCs had such a typical structure, the enlarged width of the segmentation cracks resulted in negative effects. The extended horizontal cracks attached to the segmentation cracks ran through the segment, forming bridges, and peeling off quickly during thermal cycling.

3.5 Mechanical Property

The microstructure of the YSZ coatings, including the pore structures, crack states (density, distribution, location), and crystalline grain morphology after thermal shock test changed conspicuously, which had a significant influence on the mechanical properties of the TTBCs. The Vickers hardness (H) is one of the most important factors for evaluating the durability of the TTBCs. Figure 12 shows the H values of the as-sprayed and thermally shocked coatings detected in the cross-sectional regions. The mean H values of the as-sprayed N1, N2, and N3 TTBCs were 934 ± 29 HV0.3, 944 ± 25 HV0.3, and 942 ± 28 HV0.3, respectively. The Vickers hardness of N1 coating was slightly lower than those of N2 and N3 coatings, which may be related to its coarser structure composed of high-density segmentation and branching cracks.

The effect of the grain size, combined with highly concentrated grain boundaries, resulted in a relatively higher H value. After the thermal shock tests, all the coatings manifested remarkable increase in the hardness value. The coatings were sintered during the heat treatment, resulting in a strengthening of the links between splats and healing of defects such as pores and microcracks. However, the original horizontal and vertical cracks gradually expanded and converged when exposed to the cooling stage under the superimposed thermal mismatch stress. The increases in the crack density and crack width decreased the structural strength of the coating. In addition, the average H value of the thermally shocked N2 TTBCs was significantly higher than those of the other two coatings, even after long-term thermal shock cycling. It has been verified that the completely molten regions in nanostructured coatings exhibit superior mechanical properties to those of the partially molten zones (Ref 40-42). The sintering of the nano-agglomerated powders resulted in a higher H value. Based on the previous discussion, the trend indicated that the mechanical properties were not the main cause of the coating failure.

3.6 Residual Stress

Residual stress, which functions as a crack-driving force, can accelerate the delamination and fracture of a ceramic coating (Ref 43-45). The thermal expansion mismatch between the topcoat/BC/substrate (substrate: $14\text{-}16 \times 10^{-6}/^\circ\text{C}$; topcoat: $9\text{-}10 \times 10^{-6}/^\circ\text{C}$; BC: $13\text{-}16 \times 10^{-6}/^\circ\text{C}$) fundamentally facilitated the emergence and accumulation of residual stress (Ref 46). To more intuitively and clearly analyze the thermal shock failure mechanism of N2 and N3 TTBCs, four types of stress distributions at different positions before and after thermal shock tests were measured using Raman spectroscopy, including the residual stress along the coating thickness and in the underlying ceramic layer close to the interface (20-30 μm), as shown in Fig. 13 and 14. Meanwhile, to better understand the microstructural evolution, a schematic illustration of the residual stress mechanism in the TBC system is given in Fig. 15. For the as-deposited coatings, tensile stress due to the rapid quenching effect of molten droplets (N2: 48.63 ± 5.97 MPa, N3: 40.06 ± 1.25 MPa) was present in the topcoat, and did not change significantly along the thickness direction of the ceramic coating. The Raman peak position shifted to the left when compared to that of the powder, which could be attributed to the existing residual stress in the coating (Ref 47, 48). The distribution of the tensile stress appeared to be irregular because of the anisotropic regions in N3 coating. As the experiment progressed, the residual stress in the coating transformed from tensile stress to compressive stress, and the coating thickness increased. N2 possessed a higher level of accumulated residual stress owing to its excellent thermal shock resistance. The crack propagation and creep in the BC led to stress relaxation; thus, the interfacial stress showed an almost random distribution. The local stress concentration caused lattice distortion, thereby deteriorating the coatings through spallation, regardless of the average stress (Ref 49). It is worth noting that the as-sprayed N2 TTBC had a higher tensile stress at the interface than that of the N3 TTBC, but after the thermal shock tests, the transitional compressive stress in N2 TTBCs was higher than that of N3 TTBC. This was because the tensile stress generated during the heating stage could be released continuously through the initiation and propagation of microcracks (Ref 50, 51). In particular, for N2 coating, a large

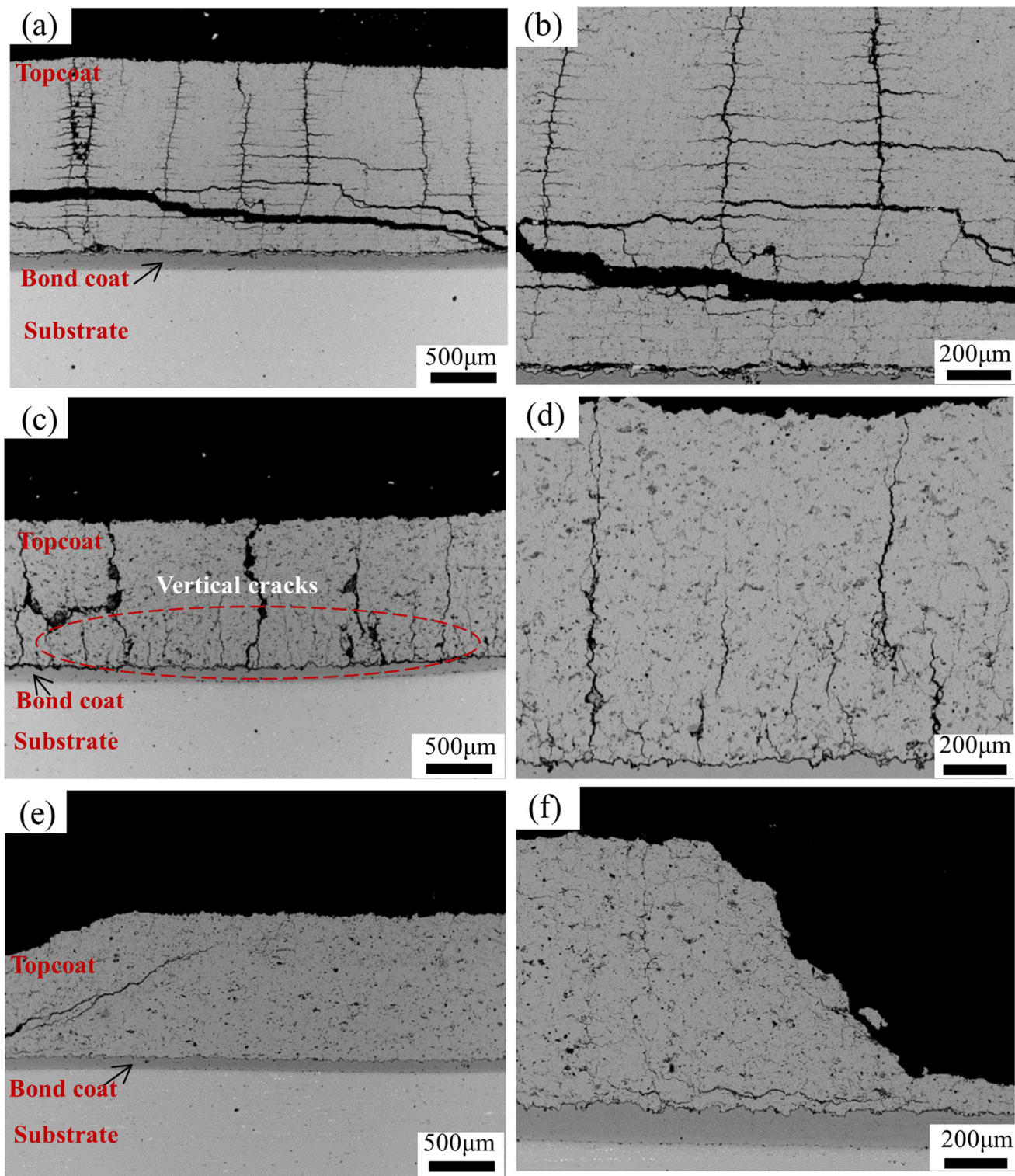


Fig. 9 Polished section morphologies (at low (left) and high (right) magnification) of TTBCs deposited using APS after thermal shock tests: (a, b) N1 coatings, (c, d) N2 coatings, and (e, f) N3 coatings

number of newly emerged vertical microcracks at the underlying part of the ceramic coating (near the topcoat/BC interface) effectively released tensile stress via crack evolution. However, the compressive stress generated during the cooling process could not be mediated by the expansion of cracks, which led to a successive increase in the accumulated compressive stress at

the interface. Tensile stress was the root cause of the spalling failure of the coating. In summary, the numerous newly generated and nonproliferative vertical cracks at the underlying part of the ceramic coating close to the interface (20-30 μm) helped to reduce the accumulation of residual stress in the coating, thereby improving the thermal cycling lifetime.

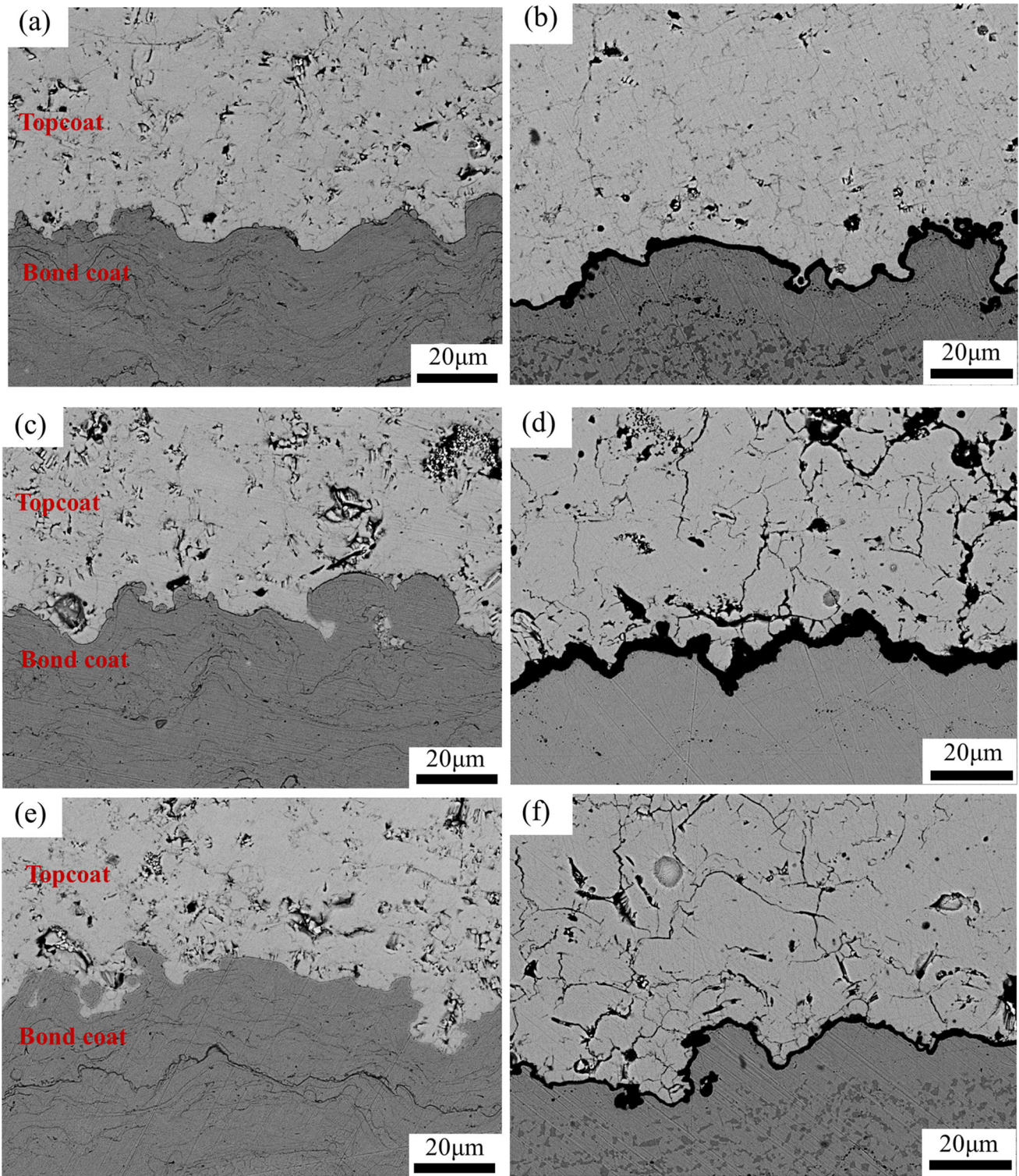


Fig. 10 Polished section morphologies of thermally grown oxide (TGO) generated at the interface: (a, c, e) as-sprayed, (b, d, f) after thermal shock test, (a, b) N1 coatings, (c, d) N2 coatings, and (e, f) N3 coatings

4. Conclusions

Three types of 8YSZ TTBCs (traditional coating, nanostructured coating, and segmentation-cracked coating) with different intrinsic cracks were fabricated via the APS process. The thermal shock behaviors, including the phase composition,

microstructure, grain growth, mechanical properties, and stress distribution of the as-sprayed coatings and thermally shocked samples were investigated systematically using a variety of characterization methods. A comparative analysis of the failure mechanisms of TTBCs deposited using APS was conducted. The main conclusions are as follows.

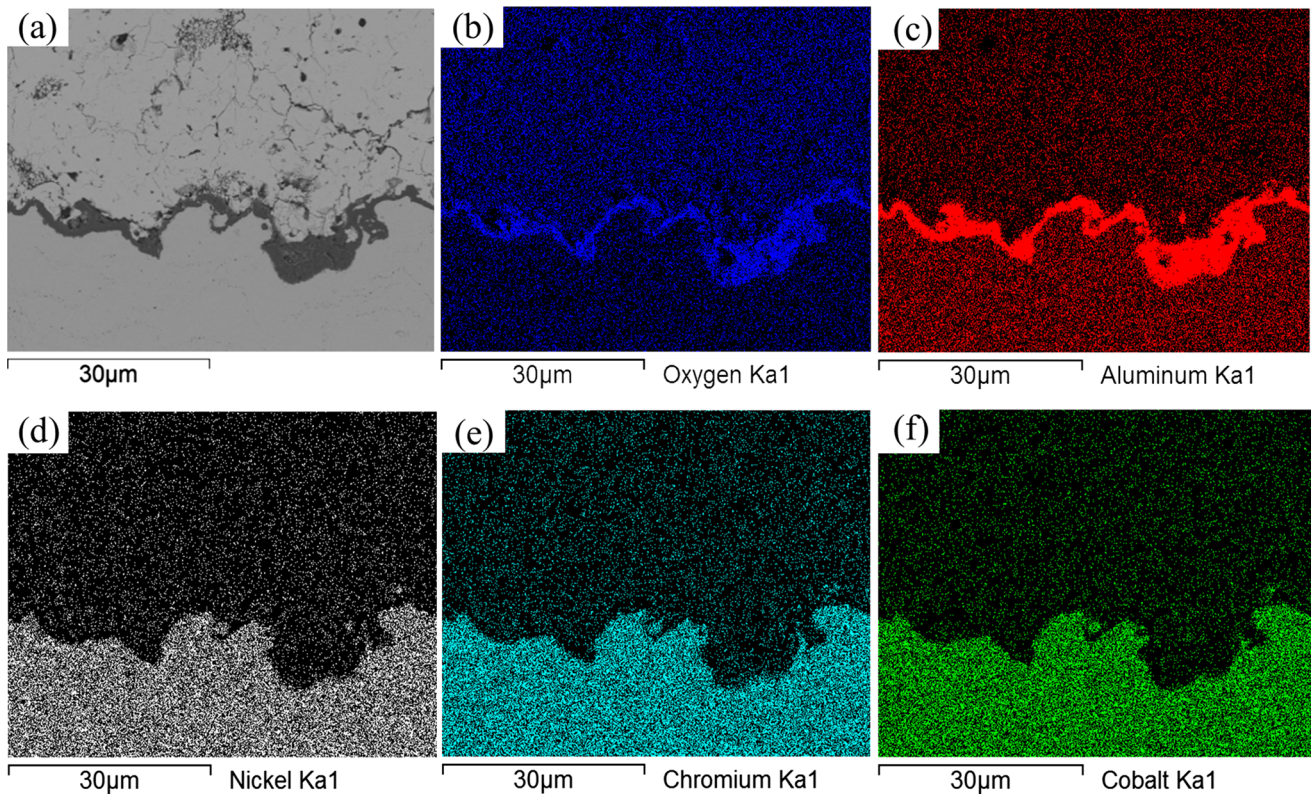


Fig. 11 Cross section and EDS map scanning results for failure zone of thermally shocked N2 coating

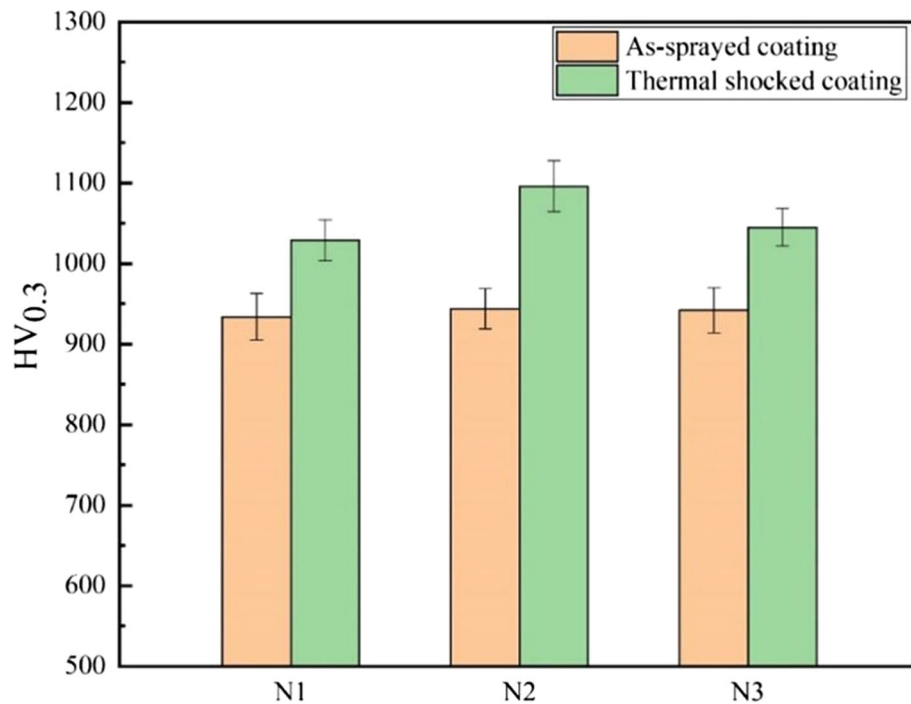


Fig. 12 Vickers hardness values of as-sprayed and heat-treated coatings

- There was a certain density of vertical cracks on the upper (near the surface of the ceramic layer) and lower (near the BC/topcoat interface) sides of the nanostructured as-sprayed TTBCs. The measured Ds of the segmentation-cracked TTBCs was 2.5 cm^{-1} , and some branch cracks were bridged. Traditional TTBCs exhibited a typical lamellar structure.
- The thermal shock resistance of the nanostructured coating (81 thermal cycles) was much higher than those of the segmented TTBCs (11 thermal cycles) and traditional

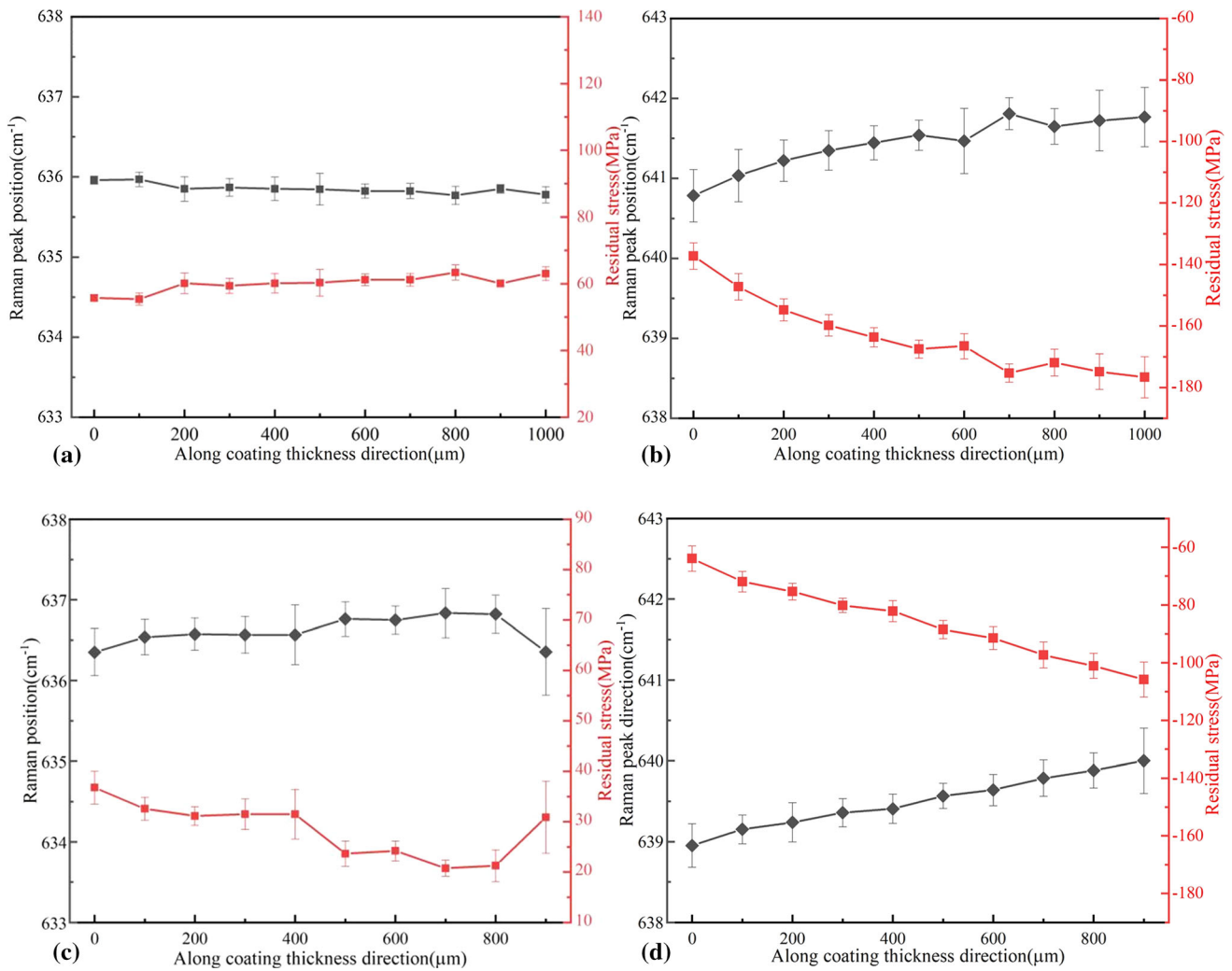


Fig. 13 Distributions of residual stress along the coating thickness: (a, c) as-sprayed samples, (b, d) thermally shocked samples, (a, b) N2 coating, and (c, d) N3 coating (positive represents tensile stress, negative represents compressive stress)

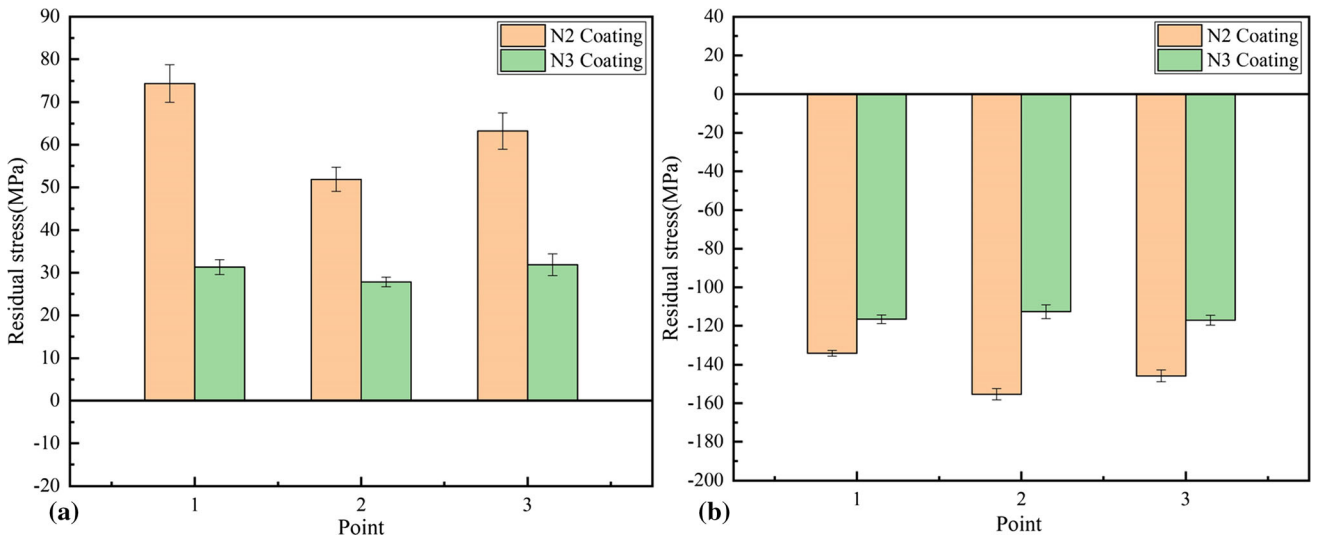


Fig. 14 Distributions of residual stress in the underlying part of ceramic layer near the topcoat/BC interface (20-30 μm) at different positions: (a) as-sprayed samples and (b) thermally shocked samples (positive indicates tensile stress, negative indicates compressive stress)

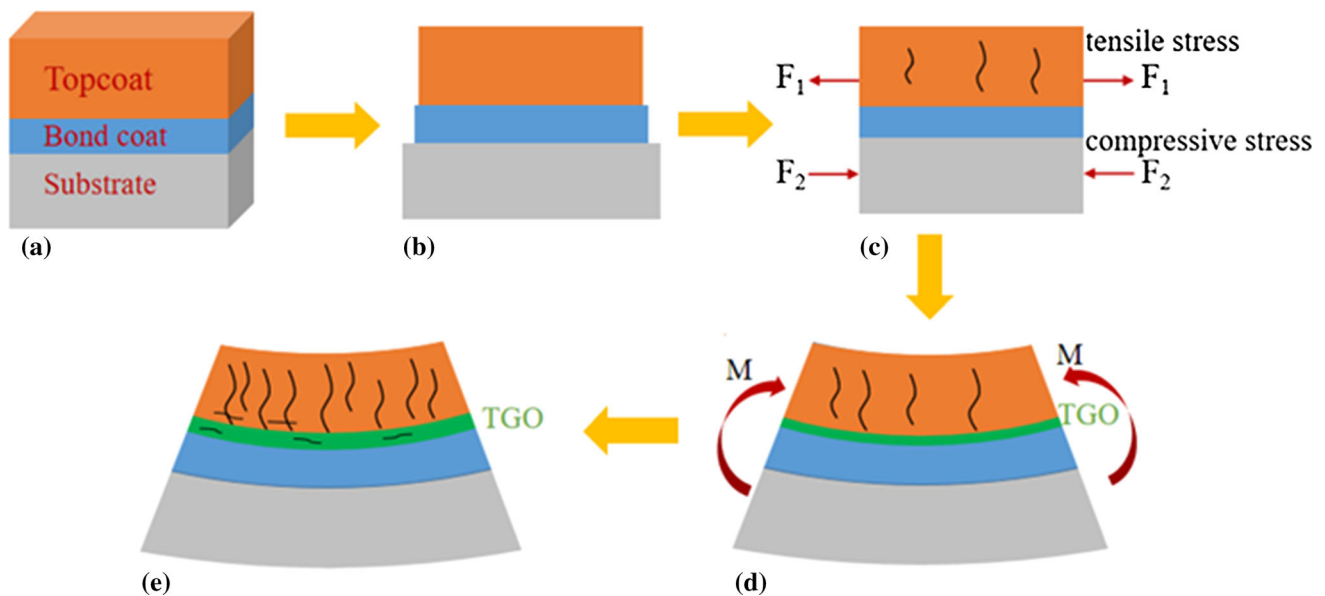


Fig. 15 Schematic illustration of the residual stress mechanism in the TBC system during heating process: (a) stress-free condition, (b) deformation caused by temperature difference, (c) interface coordination condition, (d) bending effect and moment balance, and (e) bending effect and moment balance after N thermal shock cycle

TTBCs (16 thermal cycles). The failure positions of the three coatings were different. The failure of the segmented TTBCs occurred in the topcoat owing to the propagation and penetration of branching cracks, whereas the failure of the nanostructured and traditional TTBCs mainly occurred in the underlying part of the ceramic layer.

- Crack deflection and bifurcation were governed by residual stress originating from the thermal expansion mismatch. The residual tensile stress of the as-sprayed coatings did not change significantly with the coating thickness. As the experiment progressed, the residual stress in the coating transformed from tensile stress to compressive stress, and the coating thickness increased. N2 possessed a higher level of accumulated residual stress owing to its excellent thermal shock resistance.
- The failure mechanism of TTBCs deposited using APS was most likely dominated by residual stresses generated as a result of the thermal expansion mismatch originating from adjacent parts such as the substrate and BC, and topcoat and BC, causing the initiation and propagation of cracks and accelerating the peeling of the coating. The thermally shocked N2 coatings maintained a relatively impeccable structure, indicating that a certain density of vertical cracks located at the bottom of the ceramic layer helped in prolonging the service life of the coatings.

Acknowledgments

This research was funded by the National Science and Technology Major Project (No. 2017-VI-0010-0082), the National Natural Science Foundation of China (NSFC) (No. 51701235), Science and Technology Innovation of Shanghai (No. 18511108702), the Natural Science Foundation of Shanghai (21ZR1472800), and Basic Research of the Ministry of Science and Technology of the Chinese Academy of Sciences (CXJJ-21S029).

Author's Contribution

ST and JY contributed to conceptualization; ST, JY, FS, HZ, XZ, YZ, JS, JN, and ST contributed to data curation and formal analysis; ST contributed to writing—original draft preparation; JY and ST contributed to writing—review and editing. All the authors have read and agreed to the published version of the manuscript.

References

1. D.R. Clarke and C.G. Levi, Materials Design for the Next Generation Thermal Barrier Coatings [J], *Annu. Rev. Mater. Res.*, 2003, **33**(1), p 383–417
2. N.P. Padture, M. Gell, and E.H. Jordan, Materials Science-Thermal Barrier Coatings for Gas Turbine Engine Applications [J], *Science*, 2002, **296**(5566), p 280–284
3. R. Vassen, M.O. Jarligo, T. Steinke et al., Overview on Advanced Thermal Barrier Coatings [J], *Surf. Coat. Technol.*, 2010, **205**(4), p 938–942
4. I. Gurrappa and R.A. Sambasiva, Thermal Barrier Coatings for Enhanced Efficiency of Gas Turbine Engines [J], *Surf. Coat. Technol.*, 2006, **201**, p 3016–3029
5. X. Cao, R. Vassen, and D. Stoeber, Ceramic Materials for Thermal Barrier Coatings [J], *J. Eur. Ceram. Soc.*, 2004, **24**(1), p 1–10
6. F. Shao, H. Zhao, X. Zhong et al., Characteristics of Thick Columnar YSZ Coatings Fabricated by Plasma Spray-Physical Vapor Deposition [J], *J. Eur. Ceram. Soc.*, 2018, **38**, p 1930–1937
7. C. Levi, Emerging Materials and Processes for Thermal Barrier Systems [J], *Curr. Opin. Solid State Mater. Sci.*, 2004, **8**(1), p 77–91
8. M.A. Helminiak, N.M. Yanar, F.S. Pettit, T.A. Taylor, and G.H. Meier, The Behavior of High Purity, Low Density Air Plasma Sprayed Thermal Barrier Coatings [J], *Surf. Coat. Technol.*, 2009, **204**(6–7), p 793–796
9. S. Tailor, R. Upadhyaya, S.Y. Manjunath et al., Atmospheric Plasma Sprayed 7%-YSZ thick Thermal Barrier Coatings with Controlled Segmentation Crack Densities and Its Thermal Cycling Behavior [J], *Ceram. Int.*, 2018, **44**(3), p 2691–2699
10. Z.M. Goudarzi, Z. Valefi, and P. Zamani, Effect of Functionally Graded Structure Design on Durability and Thermal Insulation Capacity of Plasma-Sprayed Thick Thermal Barrier Coating [J], *Ceram. Int.*, 2021, **47**(24), p 34361–34379

11. K. Wesling, D. Socie, and B. Beardsley, Fatigue of Thick Thermal Barrier Coatings [J], *J. Am. Ceram. Soc.*, 1994, **77**(7), p 1863–1868
12. H.D. Steffens, Z. Babiak, and M. Gramlich, Some Aspects of Thick Thermal Barrier Coating Lifetime Prolongation [J], *J. Therm. Spray Technol.*, 1998, **8**(4), p 517–522
13. P. Bengtsson, T. Ericsson, and J. Wigren, Thermal Shock Testing of Burner Cans Coated with a Thick Thermal Barrier Coating [J], *J. Therm. Spray Technol.*, 1998, **7**(3), p 340–348
14. M. Karger, R. Vassen, and D. Stover, Atmospheric Plasma Sprayed Thermal Barrier Coatings with High Segmentation Crack Densities: Spraying Process, Microstructure and thermal Cycling Behavior [J], *Surf. Coat. Technol.*, 2011, **206**(1), p 16–23
15. K. Khor, Z. Dong, and Y. Gu, Plasma Sprayed Functionally Graded Thermal Barrier Coatings [J], *Mater. Lett.*, 1999, **38**, p 437–444
16. A. Scrivani, G. Rizzi, and C. Berndt, Enhanced Thick Thermal Barrier Coatings that Exhibit Varying Porosity [J], *Mater. Sci. Eng. A*, 2008, **476**(1–2), p 1–7
17. J. De la Roche, P.A. Gomez, J.M. Alvarado-Orozco et al., Hot Corrosion and Thermal Shock Resistance of Dense-CYSZ/YSZ Bilayer Thermal Barrier Coatings Systems Applied onto Ni-Base Superalloy [J], *J. Eur. Ceram. Soc.*, 2020, **40**, p 5692–5703
18. S. Tao, J. Yang, W. Li et al., Thermal Stability of Plasma-Sprayed Thick Thermal Barrier Coatings Using Triplex Pro™-200 Torch [J], *Coatings*, 2020, **10**(9), p 1–16
19. S. Tao, J. Yang, M. Zhai et al., Thermal Stability of YSZ Thick Thermal Barrier Coatings Deposited by Suspension and Atmospheric Plasma Spraying [J], *Curr. Comput.-Aided Drug Des.*, 2020, **10**(11), p 1–13
20. K.P. Jonnalagadda, R. Eriksson, K. Yuan et al., A Study of Damage Evolution in High Purity Nano TBCs during Thermal Cycling: A Fracture Mechanics Based Modelling Approach [J], *J. Eur. Ceram. Soc.*, 2017, **37**, p 2889–2899
21. M. Izadinia, R. Soltani, M.H. Sohi et al., Effect of Segmented Cracks on TGO Growth and Life of Thick Thermal Barrier Coating Under Isothermal Oxidation Conditions [J], *Ceram. Int.*, 2020, **46**, p 7475–7481
22. Y. Huang, Y. Shen, Y. Zeng et al., EBSD Analysis of Microstructure Changes in YSZ Coatings During Thermal Cycling [J], *Ceram. Int.*, 2021, **47**, p 5559–5569
23. Z. Wei and H. Cai, Stress States and Crack Behavior in Plasma Sprayed TBCs Based on a Novel Lamellar Structure Model with Real Interface Morphology [J], *Ceram. Int.*, 2019, **45**, p 16948–16962
24. Z. Wei and H. Cai, An Innovative Model Coupling TGO Growth and Crack Propagation for the Failure Assessment of Lamellar Structured Thermal Barrier Coatings [J], *Ceram. Int.*, 2020, **46**, p 2220–2237
25. W. Weng, Z. Zheng, and Q. Li, Cracking Evolution of Atmospheric Plasma-Sprayed YSZ Thermal Barrier Coatings Subjected to Isothermal Heat Treatment [J], *Surf. Coat. Technol.*, 2020, **402**, p 1–8
26. X. Zhang, K. Zhou, H. Chen et al., Properties of Thermal Barrier Coatings made of Different Shapes of ZrO₂-7wt.%Y₂O₃ Powders [J], *Rare Metal Mater. Eng.*, 2015, **44**(6), p 1301–1306
27. J. Yin, X. Zhang, J. Feng et al., Effect of Powder Composition upon Plasma Spray-Physical Vapor Deposition of 8YSZ Columnar Coating [J], *Ceram. Int.*, 2020, **46**, p 15867–15875
28. M. Tanaka, M. Hasegawa, A. Dericioglu et al., Measurement of Residual Stress in Air Plasma-Sprayed Y₂O₃-ZrO₂ Thermal Barrier Coating System Using Micro-Raman Spectroscopy [J], *Mater. Sci. Eng. A*, 2006, **419**, p 262–268
29. L. Huang, W. Liu, and J. Xu, Effects of various Substrate Materials on Structural and Optical Properties of amorphous Silicon Nitride Thin Films Deposited by Plasma-Enhanced Chemical Vapor Deposition [J], *Chin. Opt. Lett.*, 2020, **18**(8), p 083101
30. B. Shen, H. Xiong, and X. Zhang, Post-Treatment of 351nm SiO₂ Antireflective Coatings for High Power Laser Systems Prepared by the Sol-Gel Method [J], *Chin. Opt. Lett.*, 2022, **20**(1), p 011601
31. T. Pu, W. Liu, and Y. Wang, A Novel Laser Shock Post-Processing Technique on the Laser-Induced Damage Resistance of 1 Omega HfO₂/SiO₂ Multilayer Coatings [J], *High Power Laser Sci. Eng.*, 2021, **9**, p e19
32. P. Wang, G. Qi, and Z. Pan, Fabrication of large-Area Uniform Carbon Nanotube Foams as Near-Critical-Density Targets for Laser-Plasma Experiments [J], *High Power Laser Sci. Eng.*, 2021, **9**, p e29
33. Y. Zhao, L. Wang, J. Yang et al., Thermal Aging Behavior of Axial Suspension Plasma-Sprayed Ytria-Stabilized Zirconia (YSZ) Thermal Barrier Coatings [J], *J. Therm. Spray Technol.*, 2015, **24**(3), p 338–347
34. A. Keyvani, M. Saremi, and M. Sohi, An Investigation on Oxidation, Hot Corrosion and Mechanical Properties of Plasma Sprayed Conventional and Nanostructured YSZ Coatings [J], *Surf. Coat. Technol.*, 2011, **206**(2–3), p 208–216
35. K. Amarnath, M. Jenna, LYuan, et al., Nano-Micro-Structured 6%-8% YSZ Thermal Barrier Coatings: A Comprehensive Review of Comparative Performance Analysis [J], *Coatings*, 2021, **11**, p 1474
36. L. Yang, Y. Zhou, and C. Lu, Damage Evolution and Rupture Time Prediction in Thermal Barrier Coatings Subjected to Cyclic Heating and Cooling: An Acoustic Emission Method [J], *Acta Mater.*, 2011, **59**, p 6519–6529
37. W. Mao, Y. Chen, Y. Wang et al., A Multilayer Structure Shear Lag Model Applied in the Tensile Fracture Characteristics of Supersonic Plasma Sprayed Thermal Barrier Coating Systems Based on Digital Image Correlation [J], *Surf. Coat. Technol.*, 2018, **350**, p 211–226
38. C. Deng, R. Zheng, L. Wang et al., Construction of Three-Dimensional Dynamic Growth TGO (Thermally Grown Oxide) Model and Stress Simulation of 8YSZ Thermal Barrier Coating [J], *Ceram. Int.*, 2022, **48**, p 5327–5337
39. X. Zhang, K. Zhou, J. Zhang et al., Structure Evolution of 7YSZ Thermal Barrier Coating During Thermal Shock Testing [J], *J. Inorg. Mater.*, 2015, **30**(12), p 1261–1266
40. P. Carpio, E. Rayon, L. Pawlowski et al., Microstructure and Indentation Mechanical Properties of YSZ Nanostructured Coatings Obtained by Suspension Plasma Spraying [J], *Surf. Coat. Technol.*, 2013, **220**, p 237–243
41. M. Zhai, D. Li, Y. Zhao et al., Comparative Study on Thermal Shock Behavior of Thick Thermal Barrier Coatings Fabricated with Nano-Based YSZ Suspension and Agglomerated Particles [J], *Ceram. Int.*, 2016, **153**, p 12172–12179
42. Y. Zhao, D. Li, X. Zhong et al., Thermal Shock Behaviors of YSZ Thick Thermal Barrier Coatings Fabricated by Suspension and Atmospheric Plasma Spraying [J], *Surf. Coat. Technol.*, 2014, **249**, p 48–55
43. J. Yang, L. Wang, D. Li et al., Stress Analysis and Failure Mechanisms of Plasma-Sprayed Thermal Barrier Coatings [J], *J. Therm. Spray Technol.*, 2017, **26**(5), p 809–901
44. J. Kwon, J. Kim, S. Lee et al., Microstructural Evolution and Residual Stresses of Air-Plasma Sprayed Thermal Barrier Coatings Under Thermal Exposure [J], *Surf. Rev. Lett.*, 2010, **17**(3), p 337–343
45. X. Zhao and P. Xiao, Residual Stresses in Thermal Barrier Coatings Measured by Photoluminescence Piezo-Spectroscopy and Indentation Technology [J], *Surf. Coat. Technol.*, 2006, **201**, p 1124–1131
46. H. Samadi and T. Coyle, Modeling the Build-up of Interface Stresses in Multilayer Thick Barrier Coatings [J], *J. Therm. Spray Technol.*, 2009, **18**(5–6), p 996–1003
47. J. Krogstad, M. Lepple, Y. Gao et al., Effect of Ytria Content on the Zirconia Unit Cell Parameters [J], *J. Am. Ceram. Soc.*, 2011, **94**, p 4548–4555
48. M. Gizynski, X. Chen, N. Dusautoy et al., Comparative Study of the Failure Mechanism of Atmospheric and Suspension Plasma Sprayed Thermal Barrier Coatings [J], *Surf. Coat. Technol.*, 2019, **370**, p 163–176
49. M. Rajabi, M.R. Aboutalebi, S.H. Seyedein et al., Simulation of Residual Stress in Thick Thermal Barrier Coating (TTBC) During Thermal Shock: A Response Surface-Finite Element Modeling [J], *Ceram. Int.*, 2022, **48**(4), p 5299–5311
50. J. Yang, H. Zhao, X. Zhong et al., Evolution of Residual Stresses in PS-PVD Thermal Barrier Coatings on Thermal Cycling [J], *J. Therm. Spray Technol.*, 2018, **27**(6), p 914–923
51. L. Wang, Y. Wang, X. Sun et al., Microstructure and Surface Residual Stress of Plasma Sprayed Nanostructured and Conventional ZrO₂-8wt.% Thermal Barrier Coatings [J], *Surf. Interface Anal.*, 2011, **43**(5), p 869–880

Publisher's Note Springer Nature remains neutral with regard to jurisdictional claims in published maps and institutional affiliations.